Development and validation of an open-source QCT-based finite element analysis and phase field modeling for fracture prediction in goat tibia

A Thesis Presented for the

Master of Science

Degree

The University of Tennessee, Knoxville

Debangshu Paul

August 2024

ACKNOWLEDGEMENTS

I would like to express my sincere gratitude to my thesis advisor, Dr. Truster, for his invaluable guidance and support throughout this thesis project. Dr. Truster's expertise, patience, and encouragement were instrumental in shaping this thesis and keeping me motivated.

I am also grateful to the other members of my thesis committee, Dr. Dayakar Penumadu and Dr. Nicolas Wierchem, for their insightful feedback and suggestions. Their willingness to share their knowledge and expertise significantly improved the quality of this work.

My deepest appreciation goes to Dr. Pierre-Yves Mulon and Zachariah Arwood for their collaboration, and to Robin Schlimm for her unwavering support during the research process. Their contributions were essential to the completion of this project.

Finally, I am deeply indebted to my family and friends for their unwavering love and support throughout my graduate studies. Their encouragement and understanding were invaluable during challenging times. A special thank you to my wife, Bristy Paul, for her unwavering support throughout this journey, and to my loving father, who passed away in February 2024. His inspiration for the pursuit of knowledge remains a driving force for me.

This thesis would not have been possible without the contributions of all the individuals mentioned above. I am truly grateful for their support.

ABSTRACT

Predicting mechanical responses under various load conditions is of significant interest in the field of orthopedic research. Despite an abundance of research on finite element (FE) modeling for human bones, studies specifically focusing on the tibia remain notably limited. Given that mechanical properties and structural form of goat tibiae closely mimic those of human tibiae at the region of interest (ROI), they can serve as excellent models for comparative orthopedic research. While existing literature on ovine bone research offers rich in-vivo models, it lacks a validated FE model of the tibia subjected to thorough spatial error assessment.

This thesis presents a novel open-source-based FE model of a goat tibia incorporating phase field fracture representation. The model was validated using Digital Image Correlation (DIC)-measured strain under compression, offering a valuable tool for bone biomechanics research. A model of bone geometry was constructed from a 3D quantitative computed tomography (QCT) scan of the goat tibia. Density was calculated from Hounsfield values and spatially distributed within the FE mesh. To validate this FE model, we conducted a uniaxial compression test by applying the load along the shaft axis. A DIC system provided high-resolution strain measurements across the surface of the tibia, with results found to align well with FE simulation outcomes - thus validating our elastic model.

To quantitatively predict three-dimensional fractures, we used a high-performance computing (HPC) environment to couple our elastic model with a phase field model – resulting in fracture initiation and evolution predictions that closely mirror experimental observations. This high-fidelity QCT-based approach offers a framework for personalized modeling of human tibiae enabling patient-specific analysis relating to fracture risk, implant effectiveness, and optimal treatment strategies.

TABLE OF CONTENTS

Chapter One: Introduction 1

Chapter Two: Method 3

2.1. Mechanical setup 3

2.2. DIC post processing: 5

2.3. Phantom calibration: 5

2.4. Elastic model: 7

2.4.1. Model geometry 7

2.4.2. Nodal projection of spatial properties 7

2.4.3. FE analysis 9

2.4.4. Error mapping and validation method 11

2.5. Fracture model 11

Chapter Three: Results and discussion 15

3.1. Effects of the reference critical energy release rate 25

3.2. Effects of length scale: 25

3.3. Effect of boundary conditions: 25

Chapter Four: Conclusion 28

References 29

Vita 33

LIST OF TABLES

Table 1: Parameter setting in TetGen 8

LIST OF FIGURES

Figure 1: Goat tibia (G21023) wrapped with gauze dipped in saline water along with six phantom tubes, (b) A representative CT slice of tibia and phantoms, (c) Cross section of goat tibia from 3D slicer 4
Figure 2: Experimental setup with DIC system (G21031)... 4
Figure 3: Force vs displacement for G21023 with three reference points 6
Figure 4: Relationship between the HU values and mineral density 6
Figure 5: Left - 3D FE mesh blocks of goat tibia (G21023); Right - Proximal and Distal Side sets generated for application of boundary conditions.. 8
Figure 6: Stiffness distribution of goat tibia (G21023)... 10
Figure 7: Aligned FE mesh (Red) with DIC surface point cloud (RGB)... 12
Figure 8: Displacement vs reaction force for DIC and FE data (G21023) 16
Figure 9: Displacement field comparison for goat tibia G21023 (The regions with values outside of the scale were eliminated from the contour).. 16
Figure 10: Strain field comparison for goat tibia G21023 (The regions with values outside of the scale were eliminated from the contour).. 17
Figure 11: Error Plot; Displacement error in percentage (left); Strain error (right) for G21023 (The regions with values outside of the scale were eliminated from the contour) 17
Figure 12: Displacement vs reaction force for DIC and FE data (G21031) 18
Figure 13: Displacement field comparison for goat tibia G21031 (The regions with values outside of the scale were eliminated from the contour).. 18
Figure 14: Strain field comparison for goat tibia G21031 (The regions with values outside of the scale were eliminated from the contour).. 19
Figure 15: Error Plot; Displacement error in percentage (left); Strain error (right) for G21031 (The regions with values outside of the scale were eliminated from the contour) 19
Figure 16: Reaction force vs displacement for goat tibia G21023... 20
Figure 17: Reaction force vs displacement for goat tibia G21031... 20
Figure 18: Evaluation of phase-field parameter in sample G21023 (top). Sectional view enlarged to visualize the localization of fracture (bottom) 21
Figure 19: Comparative view of fracture in Phase field model with DIC and x-ray image for sample G21023.. 22
Figure 20: Evaluation of phase-field parameter in sample G21023 (top). Sectional view enlarged to visualize the localization of fracture (bottom) 23
Figure 21: Comparative view of fracture in phase field model with DIC and x-ray image for sample G21031.. 24
Figure 22: Sensitivity analysis of critical energy release rate for G21031 26
Figure 23: Effect of length scale factor on fracture initiation... 26
Figure 24: Damage field of G21023 with load applied at the distal head.. 27

Chapter One: Introduction

Investigations into bone health and physiology aid in devising improved treatments for fractures and orthopedic injuries. This covers developments in implant materials, surgical techniques, and rehabilitation approaches. Additionally, for regenerative medicine to evolve, it is essential to understand the structure and function of bones. Even with medical progress, many challenges are faced by the researchers while making decisions about bone injuries and how best to treat them. The limitations of current treatments in entirely restoring the form and function of a bone are a source of concern for both clinicians and researchers.

The mechanical properties of bone, like other structural materials, depend on the composition. Since the composition of a bone is affected by age, different diseases, nutrition, and many other factors, predicting the mechanical behavior of the bone by measuring the bone composition has been central to skeletal studies, and majorly important in orthopedics. Fracture mechanics focuses on the limiting behavior of materials, and computational models for fracture have greatly improved in the last 50 years. Though computational models for fracture have greatly improved in the last few decades, hierarchically structured materials such as bone remain a challenge however due to various layers with different properties that tolerate damage differently [1]. Detailed characterization of specimens and subsequent mechanical testing can provide the needed input for the fracture model. A properly validated model can aid in refinements of orthopedic surgery or in the designing of novel implants.

Translational research focused on orthopedic applications such as biomedical implants carries substantial value, as the number of individuals requiring orthopedic implants are continuously increasing [2]. To combat the challenges of biocompatibility, often the research begins with in vivo modelling systems prior to human clinical trials. Appropriate in vivo investigations must closely simulate the human body; so, researchers often use large animal models such as goats and sheep [3]. Goats are an excellent model for comparative orthopedic research as the size and shape of their appendicular apparatus share similarities with the human skeleton [4], [5], [6], [7], [8], [9]. Furthermore, in terms of physical properties, size and shape, goat tibia resembles that of human tibia very closely [10]. While the finite element modeling of human bones have been available in the literature [11], [12], [13], [14], [15], [16], [17], [18], [19], [20], and few in vivo studies on goats [21], [22], there has not been any study on ovine FE modeling that considered the spatial distribution of mechanical properties. This study aims to create and calibrate the FE model of the goat tibia with proper validation and predict the initiation and propagation of fracture.

The composition of bones changes with age and different diseases [23]. The study of the tibia includes the shaft which does not have a constant thickness. At different length scales, there are discrete characteristic structural features, there has been a detailed study on how the crack growth occurs in the hierarchical structure of human bones in 2015 [24]. Because of such structure, mechanical behavior of bone cannot be predicted with accuracy if the variation of the density throughout the bone is not considered. Spatial distribution of mechanical properties that is dependent on the local density is being used in human bone research, and 3D quantitative computed tomography (QCT) based finite element analysis is the method that is commonly used for such studies. However, there is a lack of research on goat bones which can be great surrogate models for human skeletal study.

The objective of our study was to develop a comprehensive physics-based model that accurately assesses the mechanical properties and fracture behavior of goat tibiae. By leveraging this advanced modeling approach, we aim to obviate the need for experiments involving cadaver specimens or live animals, and eventually to aid human bone research. Our innovative method for analyzing goat tibiae was designed to reduce animal usage in our laboratory while simultaneously enhancing our modeling systems and fostering significant scientific advancements. This research will facilitate precise predictions regarding stress concentrations in intact tibiae under physiological loads contributing valuable insights into optimal practices for subsequent bone healing studies and the development of new orthopedic devices before initiating ex vivo and in vivo experiments.

Our novel approach combines elastic model and fracture models validated from goat tibia specimens. The first component is the elastic model that maps the spatial distribution of stiffness of a bone specimen and finds the response under load. Then, a phase field model predicts the initiation and evaluation of fracture under uniaxial compression load which is validated from the experimental data.

Phase field models have emerged as a viable fracture mechanics approach to predict crack nucleation and propagation. Correlation of apparent density and the strength of the bone was studied in 1985 [25], and later several works were conducted in this field for mapping of the experimentally measured bone density through assumed model forms to produce local property variations across the specimens [11], [13], [14], [26]. To capture the complex geometry as well as local inhomogeneous and anisotropic characteristics [27] of the tibia, 3D computed tomography (CT) scans are used to obtain the geometry and spatial density distribution. While there is a number of commercial software available for reading the data from CT scan images, this study aimed to utilize open-source software to map the mechanical properties to the 3D bone model. The software that were utilized in the process were 3D Slicer [28], MOOSE framework [29] and ParaView [30]. 3D Slicer is used to extract the nodal properties and the 3D mesh; combination of ParaView and MOOSE are utilized to prepare the finite element (FE) model, and MATLAB was used to map the nodal properties into the FE model. For calibration, the simulation results will be compared with the strain field obtained from the DIC (Digital Image Correlation), a method that is well-practiced in the literature [12], [15]. CloudCompare [31] was used to perform the comparison. With the elastic model validated using DIC, another parallel finite-element code RACCOON [32] which is specialized in phase-field for fracture was utilized to simulate the initiation and propagation of fracture. Finally, the simulation results were compared with the experimental data.

Chapter Two: Method

A three-dimensional FE mesh was generated from the QCT data and spatial material properties were assigned to the nodal cloud following the procedures detailed in [33]. Thereafter, the elastic model was validated using the displacement and strain field measured by the DIC system.

2.1. Mechanical setup

Two goat tibiae (denoted by G21023 and G21031) kept frozen at -20°C were used for experiments. The tibiae were kept intact in the legs with muscles since the muscles around the leg and the skin prevent desiccation of the bone. The tibiae were obtained from the College of Veterinary Medicine – University of Tennessee, Knoxville, TN, USA. G21023 was from the left leg of a 62.2-kg female goat and G21031 was from the left leg of a 51.4-kg female goat.

On the day of the experiment, the tibiae were defrosted and surgically removed from the whole leg and cleaned of tissue. The tibiae were embedded in PMMA (Poly methyl methacrylate) at the distal and proximal ends using 6-inch diameter PVC rings. Two custom-made metal adapters were fabricated to house the PVC-PMMA ends and facilitate the Materials Test Systems (MTS) (25 kN capacity) servo-hydraulic Universal Testing Machines (UTM) to grip the specimen. To retain the moisture, gauze dipped in saline water were used to wrap each tibia and was CT scanned using a Phillips Brilliance CT Scanner [34] along with six phantom tubes (Figure *1*). The phantom tubes were filled with K_2HPO_4 solutions with concentration from 0 to 1200 mg/cc. Scanning parameters were 120 kV, exposure of 200 mAs/slice, slice thickness 0.67 mm (equal to slice spacing) with an increment of 0.33 mm.

For DIC imaging, the tibiae were painted by matte white spray paint with black speckles. Before loading the bones to failure, tibiae were loaded within the elastic limit (Figure *2*). The proximal end was mounted to the testing machine and kept fixed, while displacement was applied at the distal end along the shaft axis. Such boundary conditions are close to one of the physiological loading conditions whereas there are plans to investigate inclined and torsional loading in the future. Displacement control loading was applied using an MTS (25 kN capacity) servo hydraulic UTM. The tibiae were initially loaded in elastic region, and then unloaded. After that, they were loaded until they failed by brittle fracture. A uniform displacement rate of 0.2 mm/min was applied throughout the experiment.

Three-dimensional DIC method was used to ascertain spatially distributed displacement along the bone surface during quasi-static compression loading in accordance with [35]. Images were captured via Vic Snap software in situ at 3 Hz frame rate using a dual camera system. Sony IMX174 2.3-megapixel grasshopper cameras equipped with 17 mm Schneider Kreuznach Citrine 1.4/17 compact lenses set at f-stop value of 5.6 (f-stop working range is 1.4-11) were mounted upon a rigid frame at a standoff distance of 0.33 m, with a baseline separation of 76 mm and a stereo angle of 14 degrees for in situ imaging. Each camera had a pixel size of 5.86 microns and 1920x1200 pixel resolution. Region of interest (ROI) scale was determined as 8.6 pixel/mm in field of view approximately 223 mm by 140 mm.

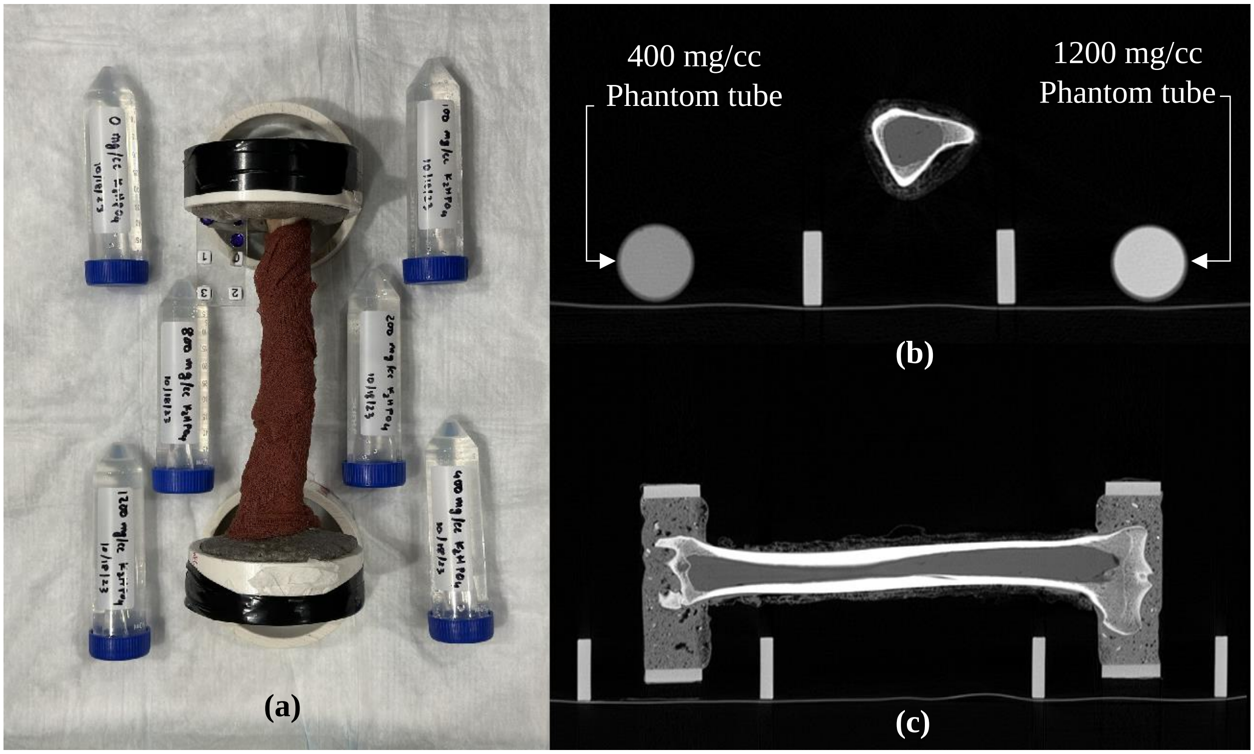

Figure 1: Goat tibia (G21023) wrapped with gauze dipped in saline water along with six phantom tubes, (b) A representative CT slice of tibia and phantoms, (c) Cross section of goat tibia from 3D slicer

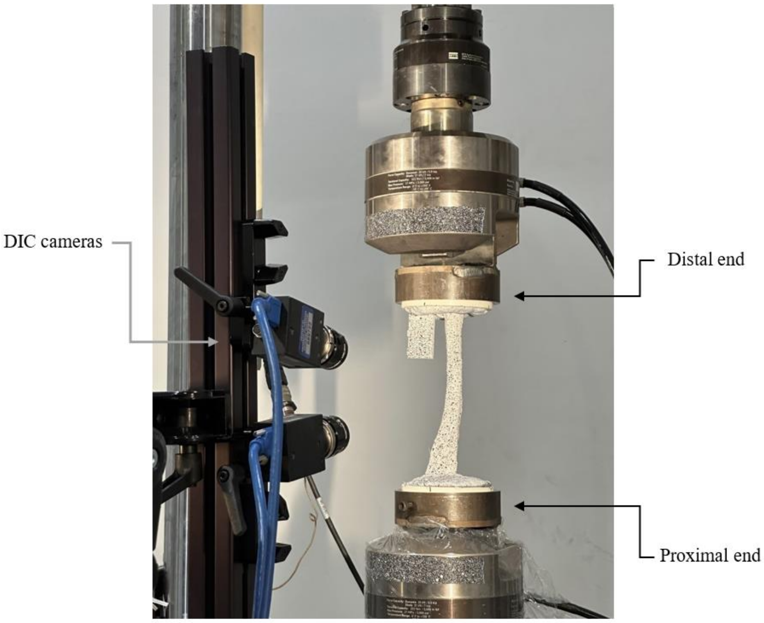

Figure 2: Experimental setup with DIC system (G21031)

2.2. DIC post processing:

Stereo calibration was performed using Correlated Solutions 9 mm 12x9 dot calibration target achieving a calibration score of 0.35, which is within the acceptable range. Data correlation was performed utilizing Vic3D software with subset size of 33 pixels and step size of 6 pixels, producing 7335 distinct correlation points with less than 0.035-pixel deviation off the epi-polar line. The subset shape function used was the fixed function in Vic 3D software package, and a filter size of 15 pixels was used for data smoothing. Lagrange strain was extracted along the coordinate directions based upon the bone orientation.

The experimental data was post processed using MATLAB scripts to determine force vs displacement relation (Figure *3*). Three instances were used as reference images within the elastic limit. Displacement applied at these three points were used in the FE model and reaction forces were compared with the experimental values. The reference image from the second of these three (image 1421) was used for the elastic model validation. Because of compliance, there were some noises recorded in the UTM, which could be identified as the bone was unloaded after loading in the elastic zone. Considering the elastic zone as a linear one, adjustments were made when the DIC and UTM data were postprocessed.

2.3. Phantom calibration:

The calibration process started with the DICOM images of the goat tibia received from the CT scanner. The property that can indicate the density is denoted as Hounsfield unit (HU) values, which needs to be calibrated to determine the density of the part being scanned. There are several studies on inter-scanner variations [19], and development of methods for calibrating the DICOM images with phantom tubes to measure the density of the bones [36], [37], [38]. Adopting from a number of works [18], [19], in this study, K_2HPO_4 at concentration of 0 mg/cc, 100 mg/cc, 200mg/cc, 400 mg/cc, 800 mg/cc, 1200 mg/cc are used for phantom calibration. The HU values of the phantom tubes are used for calibration, and a relationship between the HU value and the density is established.

Linear regression was applied to fit the following relation between ‘apparent solid density’ and HU value of the phantom tubes shown in (Equation 1.

$$\rho_{K_2HPO_4} = (0.6881x + 6.7948) \times 10^{-3}\ {}^{mg}/_{cc} \qquad \text{(Equation 1)}$$

here,
x = HU value measure by the CT scan.

This relation is used during the extraction of nodal properties from the DICOM images (Figure 4). While the tubes are marked as 100 mg/cc, 200mg/cc, 400 mg/cc, 800 mg/cc, 1200 mg/cc considering the milligrams of K_2HPO_4 powder dissolved into 50 cc of water, the actual density of the phantom tubes that were used for calculation were 96.05 mg/cc, 184.79 mg/cc, 343.46 mg/cc, 601.86 mg/cc and 803.306 mg/cc respectively. The last phantom tube was excluded from the calibration process due to the potential for abnormal values caused by the high density of the solution.

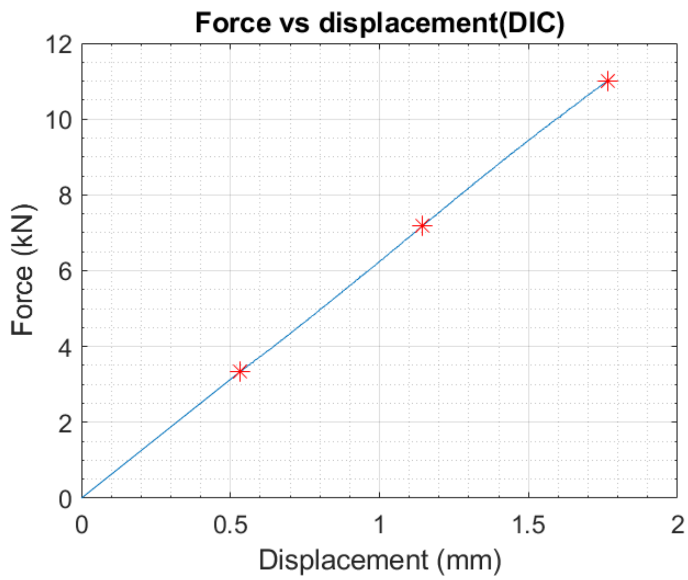

Figure 3: Force vs displacement for G21023 with three reference points

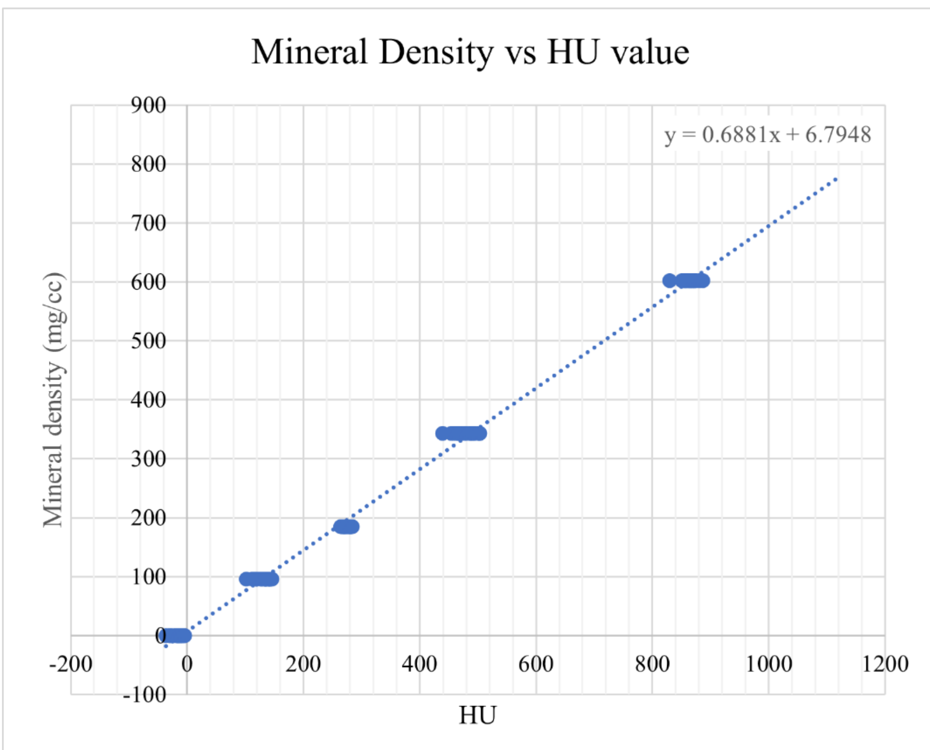

Figure 4: Relationship between the HU values and mineral density

2.4. Elastic model:

The method developed in [33] was used to obtain the model geometry and perform the elastic simulation of the FE model which are briefed in the following subsections.

2.4.1. Model geometry

The challenge of modeling bones is the heterogenous structure with inconsistent density distribution. Using the QCT data, two FE models of goat tibiae were constructed. In brief, the DICOM files were converted in to a 3D surface geometry in 3D Slicer [28] and an open-source module 'Segment Mesher', were used to create the 3D finite element mesh. The meshing method used was "TetGen" [39], and the parameters used are presented in Table *1*. The element size of the generated mesh is around 0.33mm. This study used seven mesh files, whereas three of them were used for FE analysis and the other four dummy meshes were used for creating the side sets where boundary conditions will be applied (Figure *5*). While the dummy meshes are not used in the simulation process, they are used to define the side sets at the ends and sides of the PMMAs at the distal and proximal ends by using "SideSetsBetweenSubdomainsGenerator" command in MOOSE. The two dummy meshes at the ends need to cover the extreme ends of the volume so that they can be used for calibrating the nodal projection process. The coordinate axes of the FE mesh generated by the 3D Slicer are different from those of the extracted nodal property grid from the DICOM files. Thus, calibration is required to align and scale the axes before mapping the properties.

2.4.2. Nodal projection of spatial properties

After that, a code was written in the python language and used in the python console of the 3D Slicer to create the nodal cloud of the properties in a structured grid that is later utilized to map the properties on the finite element mesh. Then, a combination of steps with MOOSE [29] and ParaView [30] was performed to prepare the FE mesh for the analysis. Apparent solid density calculated in (Equation 1) was used to evaluate the ash bone density from the relation developed in the literature [40], [41] given in ((Equation 2).

$$\rho_{ash} = 0.877 \times 1.15 \times \rho_{K_2HPO_4} + 0.08 \ {}^{gm}/_{cc}$$

(Equation 2)

While a relationship between ash density of goat tibia with Young's modulus has not yet been established, goat tibia very closely resembles human tibia in terms of mechanical properties as well as composition [42], [8]. As a result, the relationships widely used in literature [43], [44] was adopted in this study to convert the ash density to Young's modulus ((Equation 3) to (Equation 5)).

$$E_{cort-Keller} = 10200 \times \rho_{ash}^{2.01} [MPa], \rho_{ash} > 0.486$$

(Equation 3)

$$E_{const} = 2398 \ [MPa], \ 0.3 < \rho_{ash} \leq 0.486$$

(Equation 4)

$$E_{trab-Keyak} = 33900 \times \rho_{ash}^{2.2} [MPa], \rho_{ash} \leq 0.3$$

(Equation 5)

Table 1: Parameter setting in TetGen

Parameter	Value
Maximum radius-edge ratio	5
Minimum dihedral angle	10
Maximum tetrahedron volume	1

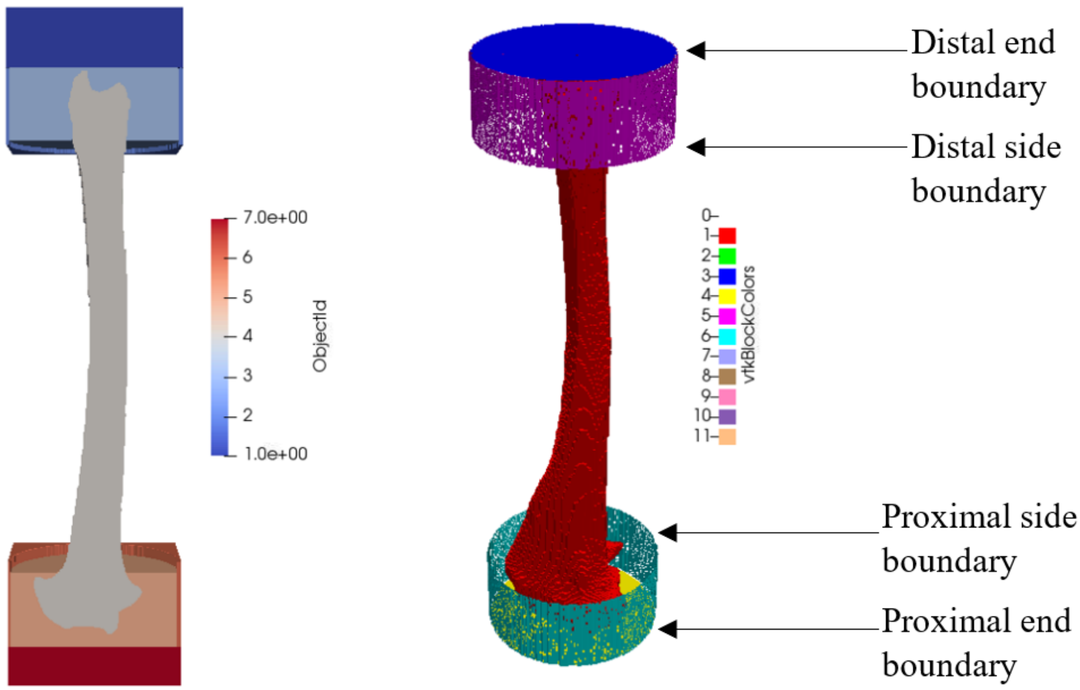

Figure 5: Left - 3D FE mesh blocks of goat tibia (G21023); Right - Proximal and Distal Side sets generated for application of boundary conditions

Poisson's ratio was set to 0.3 which has commonly been used in bone QCTFE models [32]. A finite element code was written in MATLAB to project the spatial properties from the DICOM nodal cloud to the nodes in 3D FE mesh (Figure *6*). Definition of mechanical properties for PMMA was challenging and of great significance at the same time. The experimental setup included PMMA at the two ends of the bone. The proximal end was fixed and the distal end was subjected to displacement by the UTM. The distal PMMA absorbed a substantial amount of energy and gets deformed due to compression before the load is transmitted to the distal head. Similarly, PMMA at the proximal end absorbs some energy before the fixed boundary condition is enforced by the vise. However, as PMMAs at both ends are encased in PVC rings and metal grips, only the deformation of the ROI on the tibia was measured by the DIC system. The structure of PMMA is not consistent (Figure *1*) and there is a variation of density. A linear relationship was assumed between the Young's modulus and mineral density calculated from the HU value in PMMA region considering the maximum Young's modulus as 2.9 GPa [45]. The HU value that corresponds to 2.9 GPa was determined by a parametric study, which was validated when the elastic simulation data and experimental results were compared.

2.4.3. FE analysis

It was considered that the bone behaves as a linear elastic material before accumulating enough damage and failing. To validate the model by comparing the experimental data at the elastic zone, linearized small strain theory is used for the first part of the numerical study. The FE model was then simulated in the MOOSE framework to determine the displacement and strain field under uniaxial compression load. The input file contained a ParsedMaterial object that relates the spatial stiffness with the density distribution. The function that relates the stiffness and density can be taken in the form of a function parser expression as an input parameter in the ParsedMaterial object. The nodal variable from the final exodus file generated in the previous step was used as a SolutionUserObject and the properties are parsed to generate elemental variables for the simulation [33]. The kernels, displacement variables and the material with elastic properties were constructed using the tensor mechanics master action to perform a continuum mechanics simulation. Considering that the gradient of displacement is much smaller with respect to the position, linearized small strain theory was used which is selected as a built-in option from the tensor mechanics master action. Calculations of the residual and Jacobian were handled by the stress divergence kernels reflecting the governing equations.

Displacements were prescribed from the DIC data (Figure *3*) at the distal end boundary along the bone shaft while the distal side was not allowed any movement transverse to the bone shaft axis. Proximal side and proximal end were prescribed zero displacement in all directions. Initially for sample G21023, the elastic zone of the FE model was compared with the DIC data using displacement vs reaction force at the distal end. Then, for a specific displacement of 1.143532 mm, strain and displacement fields were compared with that of the experimental data.

When the FE and experimental data are sufficiently close, the same model was used to simulate the second sample, G21031 and the results were compared with the DIC data.

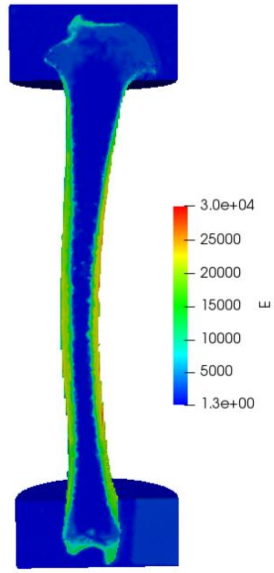

Figure 6: Stiffness distribution of goat tibia (G21023)

2.4.4. Error mapping and validation method

CloudCompare is a software that has the tools to align the mesh automatically by tracing the similar pattern in different point clouds. DIC point clouds are from the ROI on the bone, whereas the FE mesh has the point clouds of the total bone with the PMMA at the distal and proximal ends. Additionally, some artifacts generated during the segmentation process in 3D Slicer due to resolution of the CT scan. As a result, some surface features from the FE model and the DIC surface do not match. Thus, the automatic operation in CloudCompare could not be used in this study. Using the process introduced in [33], the DIC nodal cloud was manually aligned with the FE 3D mesh. Once the alignment was confirmed visually, a rotation matrix (Equation 6) can be saved and used to align any image from the DIC pixel data of the same sample (Figure 7). The ROI of DIC pixel data was trimmed as the edges had too much out of plane motion or were shadowed causing noise in the data measured by the DIC system.

$$\boldsymbol{R} = \begin{bmatrix} 0.998307 & -0.05509 & -0.01864 & 6.529131 \\ 0.054106 & 0.9973 & -0.04965 & 128.0819 \\ 0.021328 & 0.048554 & 0.998593 & -155.298 \\ 0 & 0 & 0 & 1 \end{bmatrix}$$

(Equation 6)

2.5. Fracture model

With the FE model validated by the experimental data in the linear elastic region, a phase field method was implemented to simulate the fracture behavior. RACCOON [32] is a parallel FE code specialized in phase-field for fracture. In this study RACCOON was used to simulate the fracture behavior. The framework allows combination of elasticity model and phase field model. Small strain was assumed for isotropic elasticity. Strain energy density is defined as (Equation *7*.

$$\psi^e = \frac{1}{2}Ktr(\boldsymbol{\varepsilon})^2 + Gdev(\boldsymbol{\varepsilon}): dev(\boldsymbol{\varepsilon})$$

(Equation 7)

here,

ψ^e is the strain energy, K is the bulk modulus, $\boldsymbol{\varepsilon}$ is the strain, and G is the shear modulus.

The computational framework of our mathematical model is adopted from RACCOON and MOOSE [46]. While for materials with a significant difference in behavior between volume-changing and shape-changing deformations, using a decomposition approach to differentiate between volumetric (bulk) and deviatoric (shear) contributions to the energy could provide more accurate results, the formulation is much more complex and very expensive to solve in terms of computational power and solving time. While the primary aim of this study was to investigate the fracture using the strain volumetric and deviatoric decomposition approach, due to limitation of resources and emphasizing the development of the framework, the strain was treated as a single entity without separating it into volumetric and deviatoric parts to simplify the formulation [47], [48]. In strain volumetric and deviatoric decomposition approach, the linearized strain tensor is decomposed orthogonally as shown in (Equation *8* to (Equation *10*.

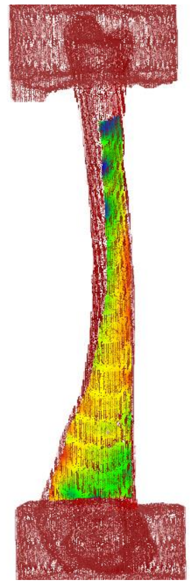

Figure 7: Aligned FE mesh (Red) with DIC surface point cloud (RGB)

$$\boldsymbol{\varepsilon} = \boldsymbol{\varepsilon}_s + \boldsymbol{\varepsilon}_D$$

(Equation 8)

$$\boldsymbol{\varepsilon_S} = \frac{1}{n}\mathrm{tr}\langle\boldsymbol{\varepsilon}\rangle^2$$

(Equation 9)

$$\boldsymbol{\varepsilon_D} = \boldsymbol{\varepsilon} - \frac{1}{n}\mathrm{tr}\langle\boldsymbol{\varepsilon}\rangle\boldsymbol{I}$$

(Equation 10)

The strain energy due to tensile and compressive stress are defined in (Equation *11* and (Equation *12*.

$$\psi^+ = \frac{1}{2}K\langle\mathrm{tr}\langle\boldsymbol{\varepsilon}\rangle^2\rangle_+ + G\boldsymbol{\varepsilon}_D \cdot \boldsymbol{\varepsilon}_D$$

(Equation 11)

$$\psi^- = \frac{1}{2}K\langle\mathrm{tr}(\boldsymbol{\varepsilon})^2\rangle_-$$

(Equation 12)

The corresponding stress is defined as in (Equation *13* and (Equation *14*.

$$\boldsymbol{\sigma}^- = K\langle\mathrm{tr}(\boldsymbol{\varepsilon})\rangle$$

(Equation 13)

$$\boldsymbol{\sigma}^+ = C\boldsymbol{\varepsilon} - \boldsymbol{\sigma}^-$$

(Equation 14)

In this work, the equations are simplified as there will not be any decomposition of strain following the approach of classical phase-field methods in [47], [48].

$$\psi^+ = \psi \text{ and } \psi^- = 0 \qquad \text{where, } \psi = g(d)\psi_0$$

Stress is redefined in (Equation *15*).

$$\boldsymbol{\sigma} = g(d)\overline{\boldsymbol{\sigma}}, \text{ where } \overline{\boldsymbol{\sigma}} = \frac{\partial\psi_0}{\partial\epsilon}$$

(Equation 15)

Crack geometry function and a quadratic degradation function were defined as shown in (Equation *16* and (Equation *17*.

$$\alpha = d^2$$

(Equation 16)

$$g(d) = (1-d)^2(1-\eta) + \eta$$

(Equation 17)

Here, α is the crack geometry function characterizes homogenous evolution of crack phase-field, and *d* is the damage field.

Here, η is a stabilization parameter, the purpose of which is not to allow the degradation to reach precisely to zero even when the damage is maximum. In this paper, $\eta = 1e - 6$ is used.

The total free energy is defined as shown in (Equation *18* to (Equation *21*):

$$F = g(d)\psi_0 + \frac{G_C}{c_0}\left(\frac{1}{l}\alpha(d) + l|\nabla d|^2\right) = f_{elastic} + f_{fracture} + \frac{G_C l}{c_0}|\nabla d|^2$$

(Equation 18)

$$f_{loc} = f_{elastic} + f_{fracture}$$

(Equation 19)

$$f_{fracture} = \frac{1}{c_0}\left(\frac{G_C}{l}\alpha(d)\right)$$

(Equation 20)

$$f_{elastic} = g(d)\psi_0$$

(Equation 21)

Here, c_0 is a scaling parameter discussed in [49], l is the length scale factor that governs the width of the crack. It is recommended to be set as minimum two times of the element size. With element size around 0.33 mm, length scale factor was varied from 0.7 to 2 to determine an appropriate value. Results from length scale factor ranging from 1 to 1.2 were shown in this study as smaller values cause convergence error and the values bigger than 1.2 result in unrealistic values.

A material kernel named ADDerivativeParsedMaterial was used to calculate the critical energy release rate at every element. A relationship between the critical energy release rate G_c and the Young's modulus E related to ash bone density ρ_{ash} was proposed as a power-law dependent one in [11] and given in (Equation *22*.

$$G_c = G_c^0 (\frac{E}{E_0})^\beta$$

(Equation 22)

here,

G_c^0 = reference critical energy release rate.

E_0 = reference critical Young's modulus.

E = local Young's modulus calculated in (Equation 3) through (Equation 5).

β = power-law exponent. $\beta = 0$ means uniform critical energy; $\beta = 1$ represents a linear relation and $\beta > 1$ implies as strong correlation between the energy release rate and Youngs modulus.

In this study, E_0 and β were assumed as 20 GPa and 0.8 according to [11], while G_c^0 was calibrated for goat tibia sample G21023. Then, the same parameter was applied on G21031 phase field model to observe its agreement with the experimental data.

Chapter Three: Results and discussion

Validation started with the FE model simulated in the linear elastic zone of goat tibia G21023. The tibia under axial compression experience rotations of the shaft due to the nonuniform thickness and stiffness (Figure 6). The PVC rings at the two ends were firmly gripped by the UTM to ensure there is no lateral and rotational movement. As a result, torque was generated at the ends of the tibia. The value of the torque was very small (about 1 kN-mm) and was not considered for the FE model as it was not in the scope of the study.

The reaction force at distal end demonstrated very close agreement with the experimental data (Figure *8*). To further verify the local behavior, displacement and strain field from the FE simulation were compared (Figure *9* and Figure *10*). While displacement fields were very closely matched, there were some deviations observed in the strain fields. The deviations are large at the sides which can be caused by out of plane motion caused by the rotation which is a weakness for a two-camera DIC system.

To have a closer look at the deviations, the errors were plotted in Figure 11. The displacement field shows an error within ±10% and strain deviations are from -0.0002 to +0.001. Considering the out of plane motion captured by a two-camera DIC system and complex shape of the goat tibia, the FE model in linear elastic zone mimics the experimental behavior very closely.

A similar procedure was implemented for goat tibia G21031 (Figure *12* to Figure 15). The displacement vs force curves exhibit slight deviation, but the linear region of the DIC data matches the FE data. The displacement field shows an error within -2.5% to 10% and strain deviations are within -0.00175 to +0.0003, which implies a good agreement between FE and experimental data. The agreement between FE elastic model and experimental data in the linear elastic zone validates the spatial property assignment of both the samples. Next, the phase-field simulation results were compared with the experimental data. The reaction force was plotted against displacement as displacement was applied at the distal end (Figure *16* and Figure *17*).

For G21023, the experimental fracture load is 13.9 kN compared to 12.3 kN from phase-filed result with an 11% error, whereas the fracture displacement is 2.25 mm from the phase-field model when compared to the experimental value of 2.43 mm with an error of 8%. For G21031, the experimental fracture load is 9.3 kN compared to 10.3 kN from phase field result with a 10% error. The fracture displacement is 2.46 mm in phase-field model, whereas the experimental value was 2.41 mm with an error of 2%.

Figure 18 illustrates the evolution of phase-field parameter in G21023. It is apparent that it localizes at a point and as it reaches the maximum value of 1, it exhibits the appearance of a fracture. A correlative analysis between X-ray imagery and post-failure photographs of the goat tibia with Phase Field model data is presented in Figure 19. The congruence between the modeled failure site and experimental observations is apparent, indicating that the phase field model replicates the experimentally observed fracture behavior. The initiation of fracture occurs within the cortical bone, proceeding to propagate transversely along the axis of the bone shaft.

Figure *20* presents a detailed depiction of the phase-field parameter evolution within specimen G21031. In Figure *21*, a rigorous comparison is conducted between X-ray and photographic documentation of the failed goat tibia and the corresponding results from phase field simulations. It is observed that the fracture onset occurs within a consistent region. The stress is concentrated in the cortical zone, where the fracture was initiated and subsequently propagated in a transverse direction through the tibial shaft.

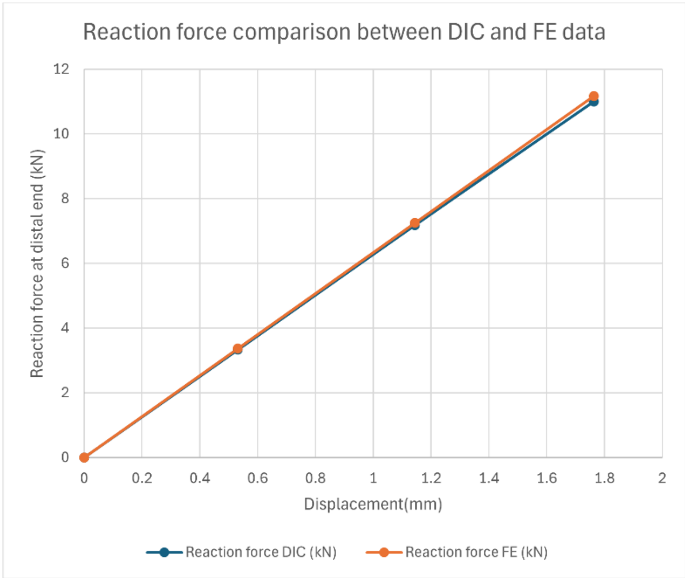

Figure 8: Displacement vs reaction force for DIC and FE data (G21023)

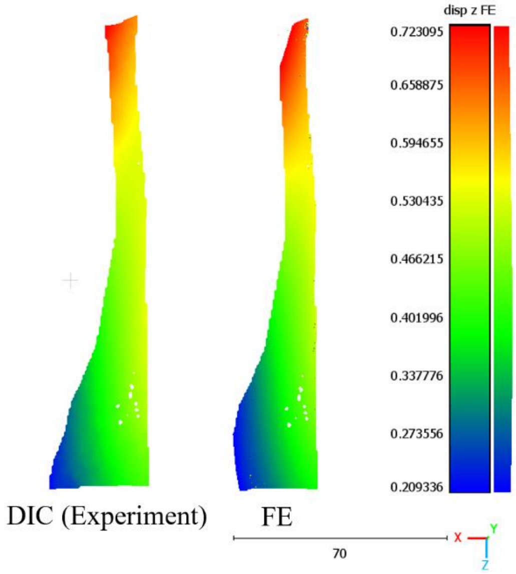

Figure 9: Displacement field comparison for goat tibia G21023 (The regions with values outside of the scale were eliminated from the contour)

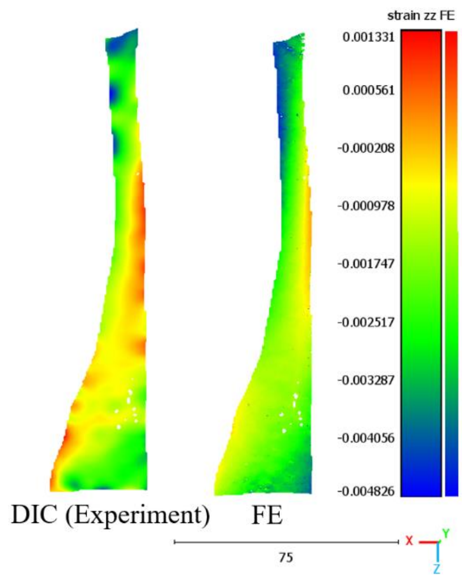

Figure 10: Strain field comparison for goat tibia G21023 (The regions with values outside of the scale were eliminated from the contour)

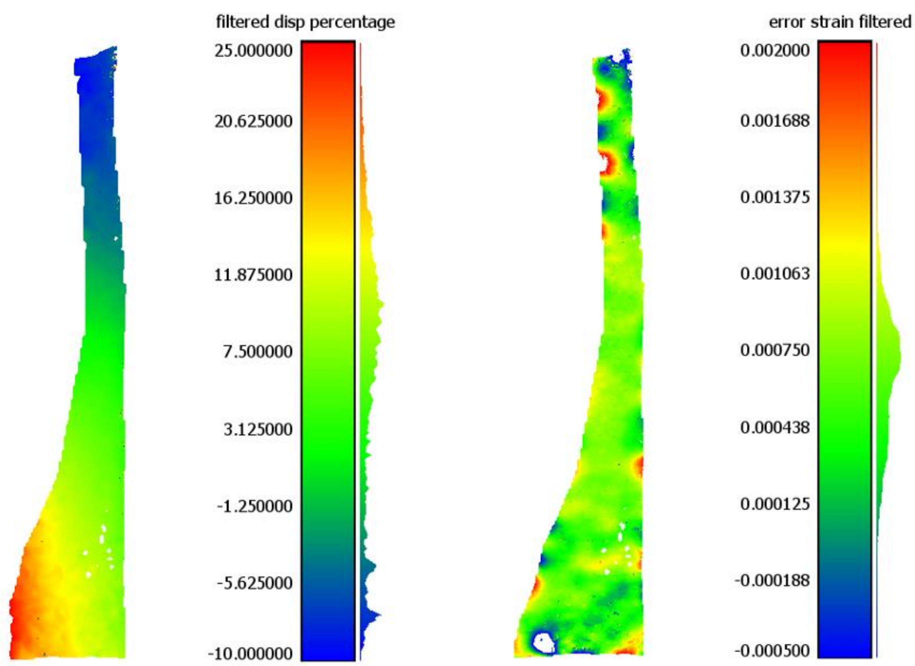

Figure 11: Error Plot; Displacement error in percentage (left); Strain error (right) for G21023 (The regions with values outside of the scale were eliminated from the contour)

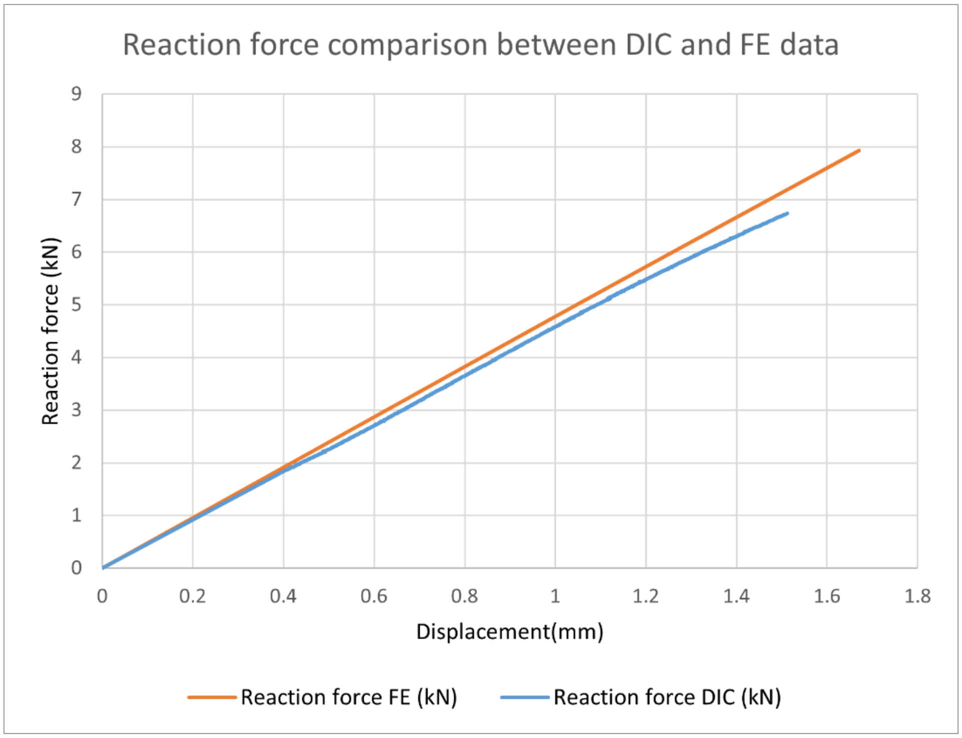

Figure 12: Displacement vs reaction force for DIC and FE data (G21031)

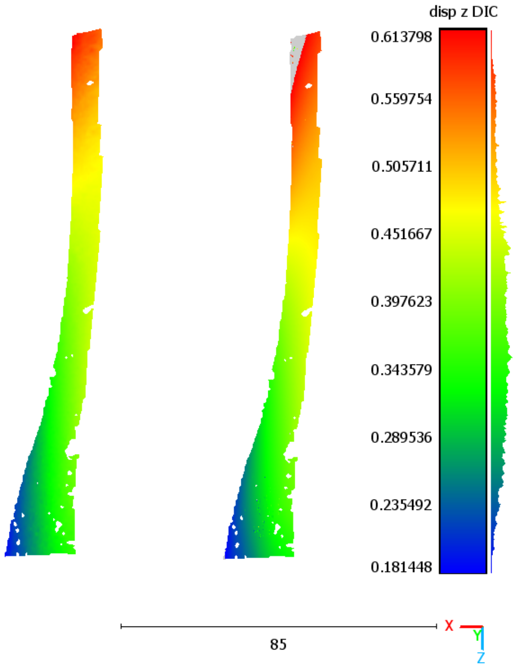

Figure 13: Displacement field comparison for goat tibia G21031 (The regions with values outside of the scale were eliminated from the contour)

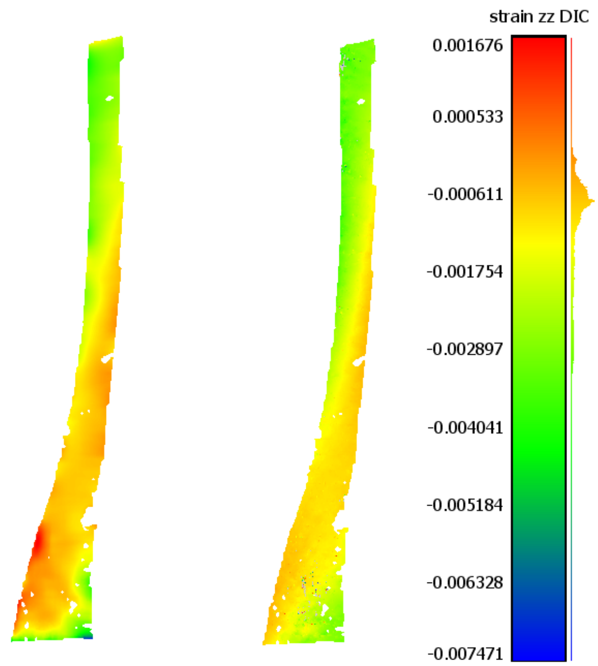

Figure 14: Strain field comparison for goat tibia G21031 (The regions with values outside of the scale were eliminated from the contour)

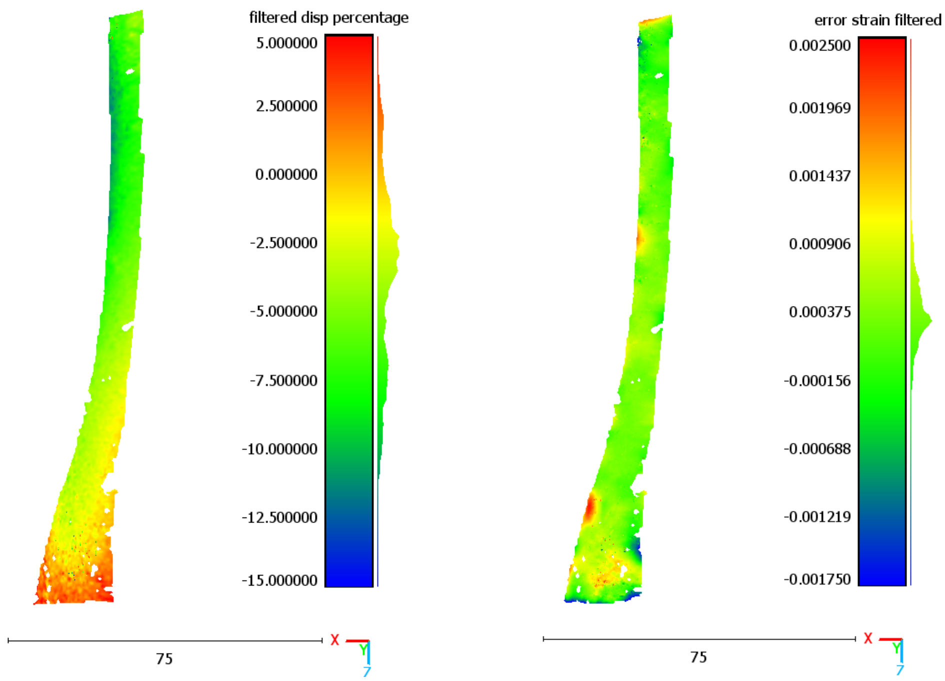

Figure 15: Error Plot; Displacement error in percentage (left); Strain error (right) for G21031 (The regions with values outside of the scale were eliminated from the contour)

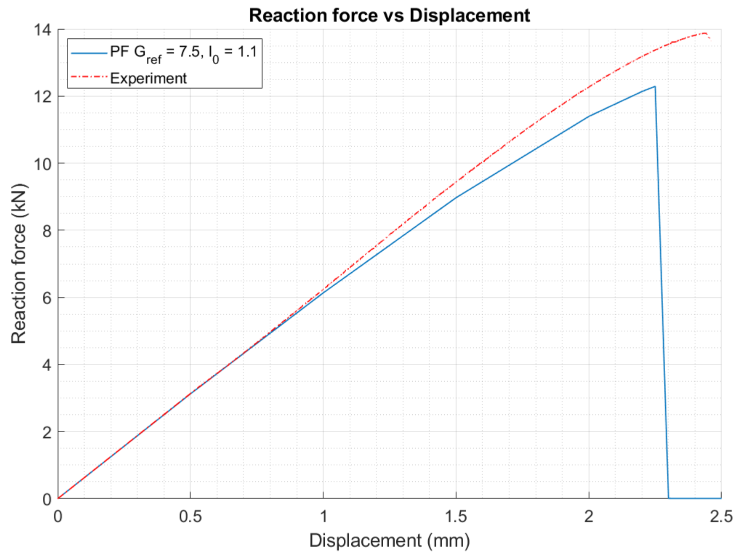

Figure 16: Reaction force vs displacement for goat tibia G21023

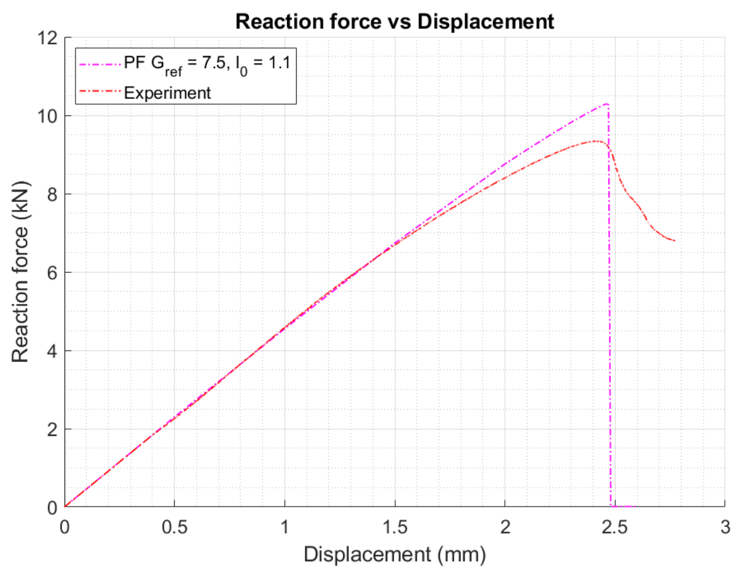

Figure 17: Reaction force vs displacement for goat tibia G21031

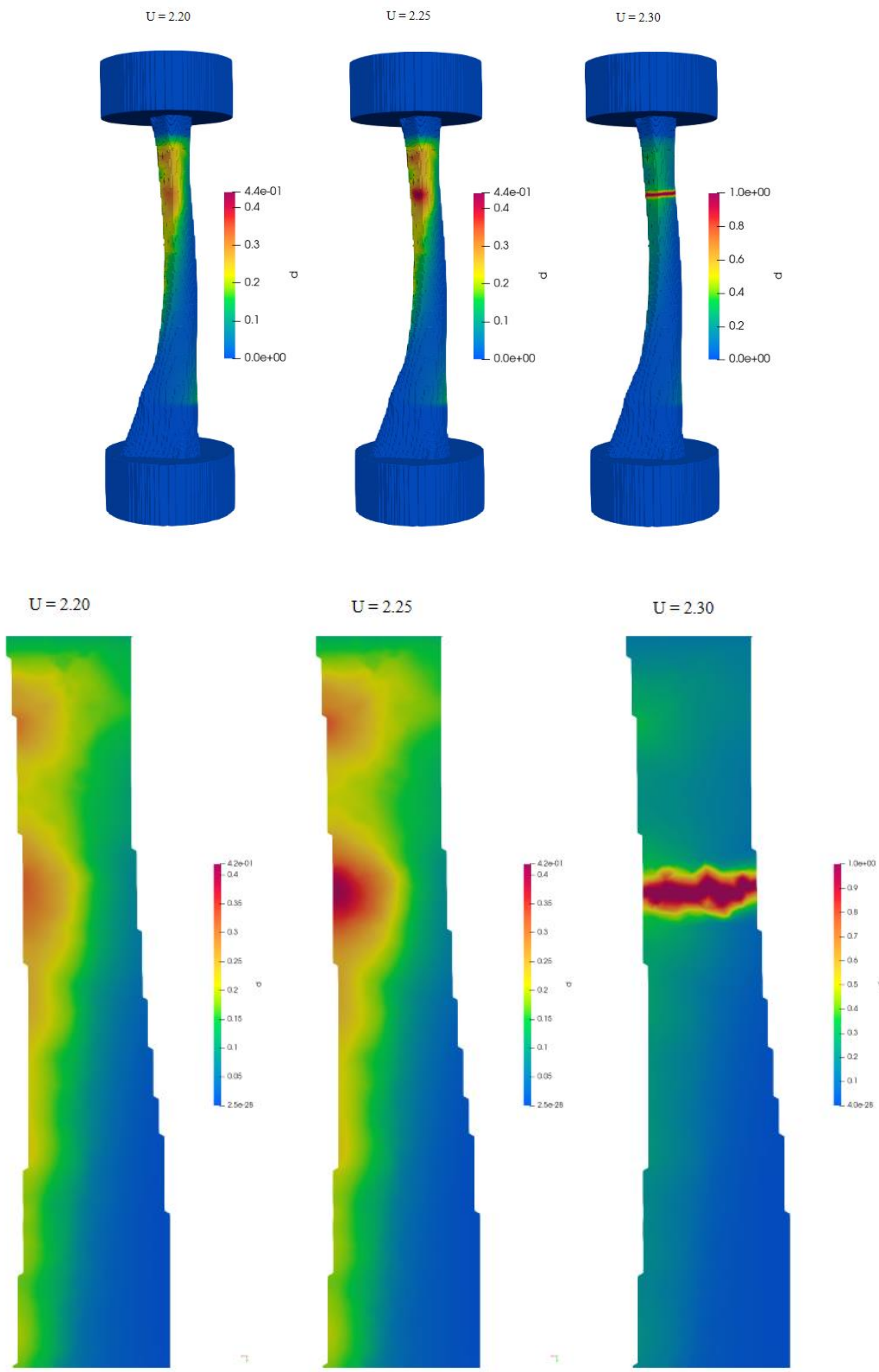

Figure 18: Evaluation of phase-field parameter in sample G21023 (top). Sectional view enlarged to visualize the localization of fracture (bottom)

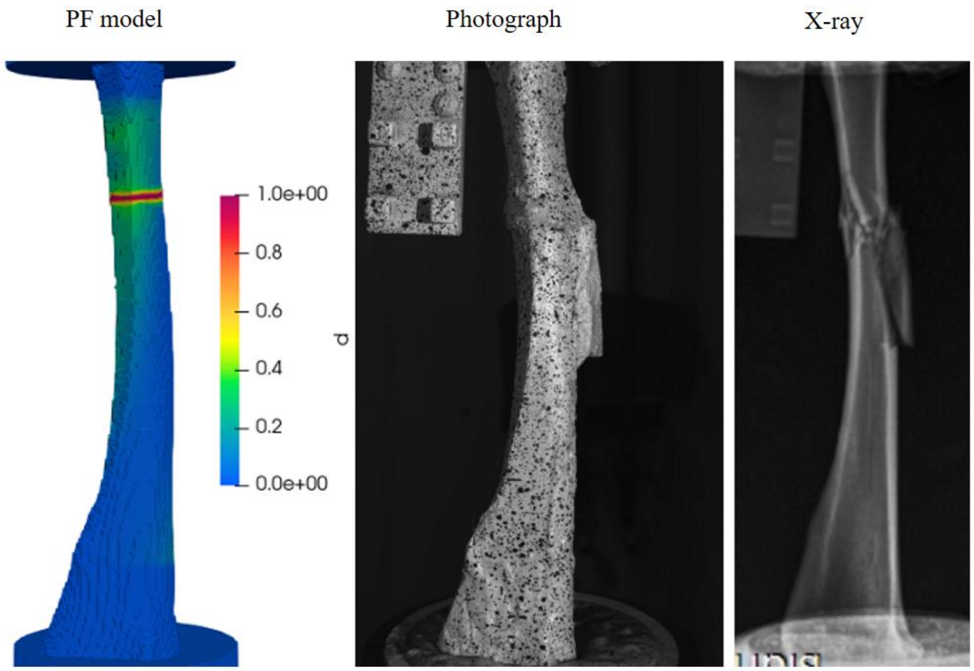

Figure 19: Comparative view of fracture in Phase field model with DIC and x-ray image for sample G21023

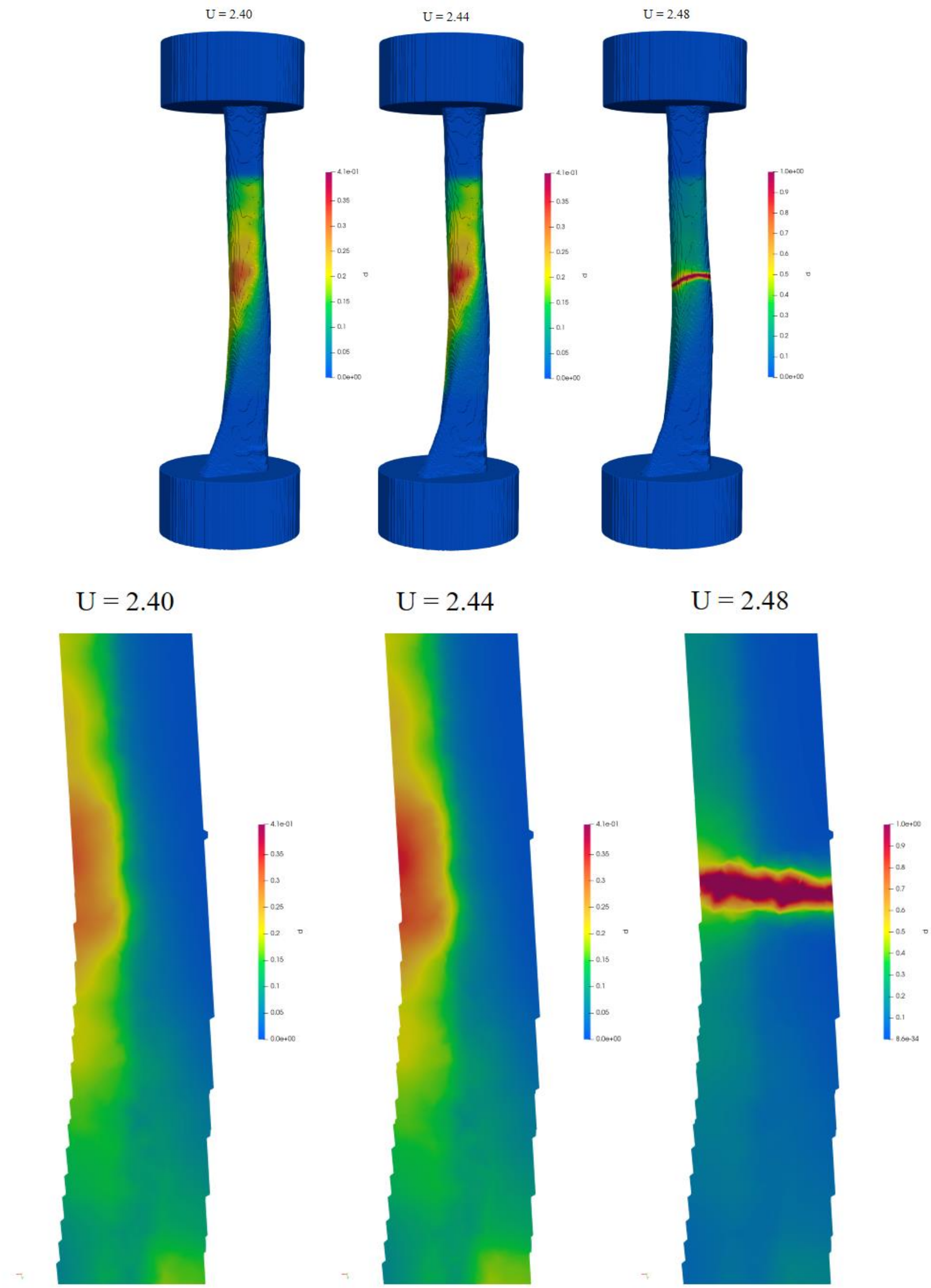

Figure 20: Evaluation of phase-field parameter in sample G21023 (top). Sectional view enlarged to visualize the localization of fracture (bottom)

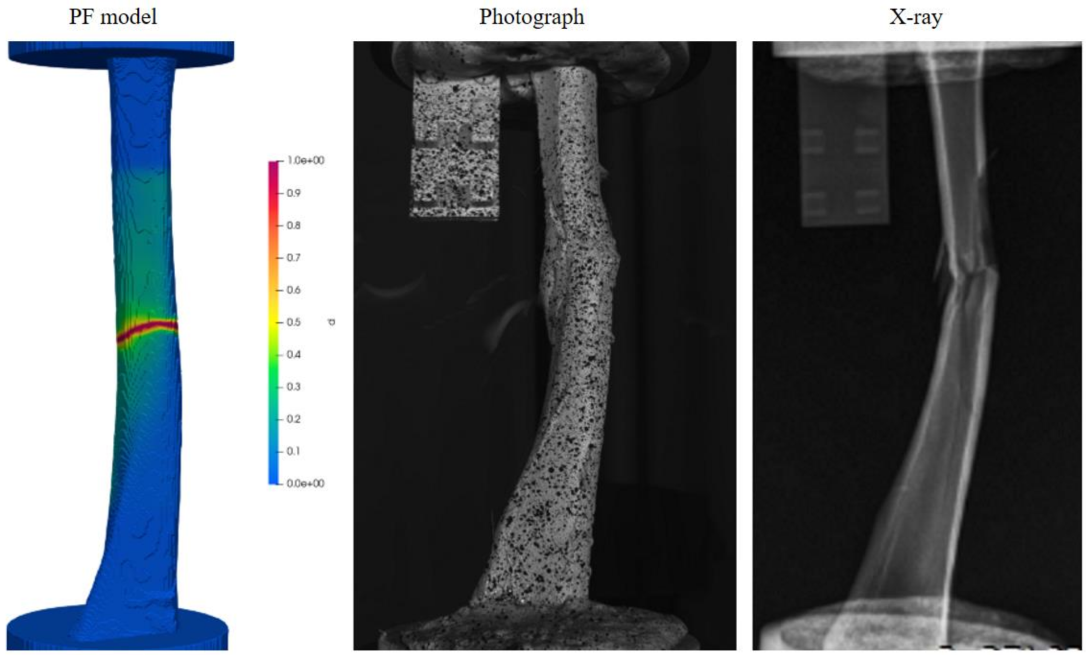

Figure 21: Comparative view of fracture in phase field model with DIC and x-ray image for sample G21031

3.1. Effects of the reference critical energy release rate

This work utilized the power-law dependence equation proposed in [11] with the beta = 0.8, and calibrated for the critical energy release rate. Figure *22* illustrates how the failure load changes with the variation of the reference critical energy release rate keeping the relationship with stiffness as discussed in Section 2.5 (Equation *22*). As the reference critical energy release rate increases the fracture load and displacement increase which is expected as the critical energy release rate is scaled by this value, and it describes the minimum amount of energy required per unit of new crack area created for a crack to propagate in a material. A value of 7.5 Jm^{-2} was adopted as the critical energy release rate for the validation process, which is close to the value of 7 Jm^{-2} that was used in [11], [12].

3.2. Effects of length scale:

The effect of length scale, l_0 was studied in this section. Material strength and response are greatly impacted by the length scale. The effect of this is illustrated in (Figure 23), and for this work the value of 1.1 was adopted. The size of the element that was used in this study was approximately 0.33 mm. The length scale needs to be at least two elements across the width and should be as small as possible [11]. The comparison was shown for length scales of 1.0, 1.1 and 1.2. The crack pattern does not change significantly except smaller value yields sharper cracks. However, it affects the convergence, and it was observed that the fracture load and fracture displacement increase with decreasing length scale.

3.3. Effect of boundary conditions:

To investigate the appropriateness of application of boundary conditions, another simulation was performed by applying load directly on the distal head of the goat tibia G21023 (Figure 24). The fracture location shifts towards the distal end further from the actual location, indicating the method of applying load on the PMMA, keeping resemblance with the experimental setup, is a more appropriate modeling approach.

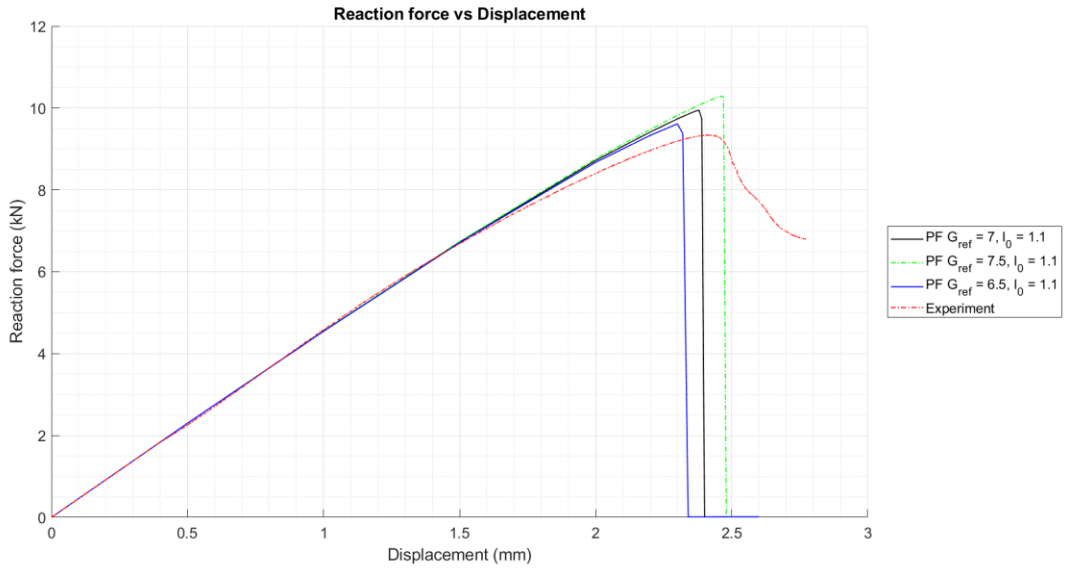

Figure 22: Sensitivity analysis of critical energy release rate for G21031

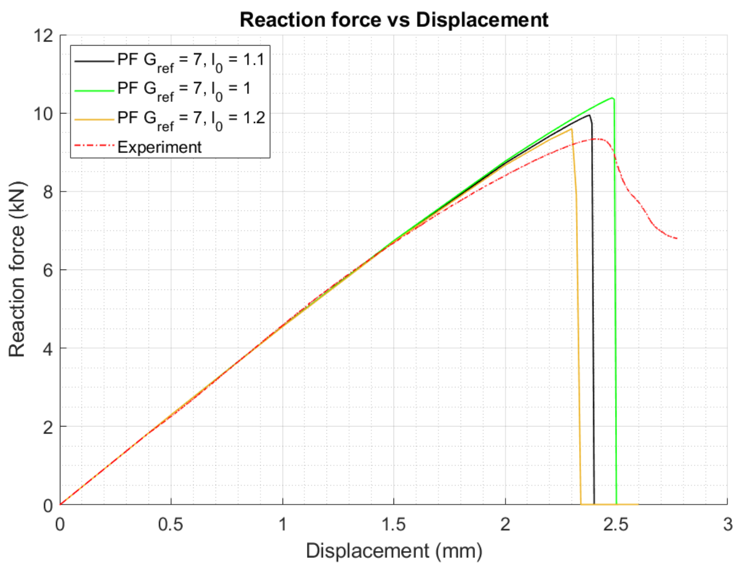

Figure 23: Effect of length scale factor on fracture initiation

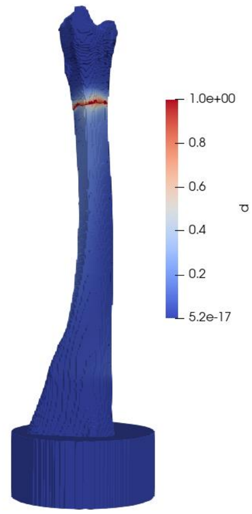

Figure 24: Damage field of G21023 with load applied at the distal head

Chapter Four: Conclusion

In this study, a novel open-source FE-based model of a goat tibia incorporating phase field fracture representation was presented. A 3D FE mesh was prepared from the QCT data of two goat tibiae. The heterogenous structure of the bone was replicated by projecting the nodal properties evaluated from the local densities that were correlated with the HU values from CT data. For the displacement field, the first sample had an error within ±10%, whereas the second sample had error ranging from -2.5% to 10%. The strain field varied from a minimum value of approximately -0.00175 to +0.001. After validating the elastic model, the FE model was used in a phase-field simulation. Finally, the fracture behaviors were found to have a good agreement with the experimental data. The phase-field model predicted the fracture load with about 90% accuracy for both samples, whereas the fracture load was predicted with an accuracy of 92% and 98% for the two samples respectively. The comparative image analysis indicates that the phase field model mimics the experimental scenario very closely.

With available scope, a few more additional specimens can be used for the experiment with force applied at an angle different to the shaft axis as well as torsional loading. The developed framework should be able to predict such loading conditions, and minor variations can be calibrated to develop a model that can simulate the physiological loading scenarios of the goat tibia. A low-cost method should be investigated to utilize the strain deviatoric and volumetric energy split approach, which should be able to capture the fracture behavior more accurately.

There is a wealth of extensive in-vivo studies concerning ovine bones, alongside research employing FE modeling for human bones. By leveraging a phase-field method previously validated with human bones, we have developed an FE model for goat tibiae. This novel application serves not only to bridge a gap in the existing literature but also to lay the groundwork for expansive research within this domain. The utility of our model extends to enhancing computational predictions pertinent to risk factors' impact assessment, surgical model design optimization, and the innovation of new surgical implants and techniques. Moreover, it can conserve resources by lowering the dependence on first ex vivo and second in vivo pilot research modeling while offering these insights.

References

[1] A. Ural, “Advanced Modeling Methods—Applications to Bone Fracture Mechanics,” *Curr. Osteoporos. Rep.*, vol. 18, no. 5, pp. 568–576, Oct. 2020, doi: 10.1007/s11914-020-00615-1.

[2] R. M. Grzeskowiak, J. Schumacher, M. S. Dhar, D. P. Harper, P.-Y. Mulon, and D. E. Anderson, “Bone and Cartilage Interfaces With Orthopedic Implants: A Literature Review,” *Front. Surg.*, vol. 7, p. 601244, Dec. 2020, doi: 10.3389/fsurg.2020.601244.

[3] K. M. Roux, L. H. Cobb, M. A. Seitz, and L. B. Priddy, “Innovations in osteomyelitis research: A review of animal models,” *Anim. Models Exp. Med.*, vol. 4, no. 1, pp. 59–70, Mar. 2021, doi: 10.1002/ame2.12149.

[4] B. Karakilic, E. Taskiran, B. Doganavsargil, B. Uzun, S. Celik, and E. Kaya Bicer, “Central defect type partial ACL injury model on goat knees: the effect of infrapatellar fat pad excision,” *J. Orthop. Surg.*, vol. 10, no. 1, p. 137, Dec. 2015, doi: 10.1186/s13018-015-0281-x.

[5] A. L. Bascuñán, A. Biedrzycki, S. A. Banks, D. D. Lewis, and S. E. Kim, “Large Animal Models for Anterior Cruciate Ligament Research,” *Front. Vet. Sci.*, vol. 6, p. 292, Aug. 2019, doi: 10.3389/fvets.2019.00292.

[6] R. F. LaPrade, K. A. Kimber, F. A. Wentorf, and E. J. Olson, “Anatomy of the posterolateral aspect of the goat knee,” *J. Orthop. Res.*, vol. 24, no. 2, pp. 141–148, Feb. 2006, doi: 10.1002/jor.20032.

[7] B. L. Proffen, M. McElfresh, B. C. Fleming, and M. M. Murray, “A comparative anatomical study of the human knee and six animal species,” *The Knee*, vol. 19, no. 4, pp. 493–499, Aug. 2012, doi: 10.1016/j.knee.2011.07.005.

[8] J. Aerssens, S. Boonen, G. Lowet, and J. Dequeker, “Interspecies Differences in Bone Composition, Density, and Quality: Potential Implications for in Vivo Bone Research,” vol. 139, no. 2, 1998.

[9] L. Martini, M. Fini, G. Giavaresi, and R. Giardino, “Sheep Model in Orthopedic Research: A Literature Review,” *Comp. Med.*, vol. 51, no. 4, 2001.

[10] C. Christou, R. A. Oliver, M. H. Pelletier, and W. R. Walsh, “Ovine Model for Critical-Size Tibial Segmental Defects,” *Comp. Med.*, vol. 64, no. 5, 2014.

[11] R. Shen, H. Waisman, Z. Yosibash, and G. Dahan, “A novel phase field method for modeling the fracture of long bones,” *Int. J. Numer. Methods Biomed. Eng.*, vol. 35, no. 8, Aug. 2019, doi: 10.1002/cnm.3211.

[12] L. Hug, G. Dahan, S. Kollmannsberger, E. Rank, and Z. Yosibash, “Predicting fracture in the proximal humerus using phase field models,” *J. Mech. Behav. Biomed. Mater.*, vol. 134, p. 105415, Oct. 2022, doi: 10.1016/j.jmbbm.2022.105415.

[13] J. H. Keyak, M. G. Fourkas, J. M. Meagher, and H. B. Skinner, “Validation of an automated method of three-dimensional finite element modelling of bone,” *J. Biomed. Eng.*, vol. 15, no. 6, pp. 505–509, Nov. 1993, doi: 10.1016/0141-5425(93)90066-8.

[14] C. M. Les, J. H. Keyak, S. M. Stover, K. T. Taylor, and A. J. Kaneps, “Estimation of material properties in the equine metacarpus with use of quantitative computed tomography,” *J. Orthop. Res.*, vol. 12, no. 6, pp. 822–833, Nov. 1994, doi: 10.1002/jor.1100120610.

[15] G. Dahan, O. Safran, and Z. Yosibash, “Can neck fractures in proximal humeri be predicted by CT-based FEA?,” *J. Biomech.*, vol. 136, p. 111039, May 2022, doi: 10.1016/j.jbiomech.2022.111039.

[16] Z. Yosibash, R. Padan, L. Joskowicz, and C. Milgrom, “A CT-Based High-Order Finite Element Analysis of the Human Proximal Femur Compared to In-vitro Experiments,” *J. Biomech. Eng.*, vol. 129, no. 3, pp. 297–309, Jun. 2007, doi: 10.1115/1.2720906.

[17] Z. Yosibash, R. Plitman Mayo, G. Dahan, N. Trabelsi, G. Amir, and C. Milgrom, “Predicting the stiffness and strength of human femurs with real metastatic tumors,” *Bone*, vol. 69, pp. 180–190, Dec. 2014, doi: 10.1016/j.bone.2014.09.022.

[18] G. Dahan, N. Trabelsi, O. Safran, and Z. Yosibash, “Finite element analyses for predicting anatomical neck fractures in the proximal humerus,” *Clin. Biomech.*, vol. 68, pp. 114–121, Aug. 2019, doi: 10.1016/j.clinbiomech.2019.05.028.

[19] Y. Katz, G. Dahan, J. Sosna, I. Shelef, E. Cherniavsky, and Z. Yosibash, “Scanner influence on the mechanical response of QCT-based finite element analysis of long bones,” *J. Biomech.*, vol. 86, pp. 149–159, Mar. 2019, doi: 10.1016/j.jbiomech.2019.01.049.

[20] G. Dahan, N. Trabelsi, O. Safran, and Z. Yosibash, “Verified and validated finite element analyses of humeri,” *J. Biomech.*, vol. 49, no. 7, pp. 1094–1102, May 2016, doi: 10.1016/j.jbiomech.2016.02.036.

[21] R. P. Main and A. A. Biewener, “In Vivo Bone Strain and Ontogenetic Growth Patterns in Relation to Life-History Strategies and Performance in Two Vertebrate Taxa: Goats and Emu,” *Physiol. Biochem. Zool.*, vol. 79, no. 1, pp. 57–72, Jan. 2006, doi: 10.1086/498184.

[22] R. P. Main and A. A. Biewener, “Ontogenetic patterns of limb loading, *in vivo* bone strains and growth in the goat radius,” *J. Exp. Biol.*, vol. 207, no. 15, pp. 2577–2588, Jul. 2004, doi: 10.1242/jeb.01065.

[23] A. L. Boskey, “Bone composition: relationship to bone fragility and antiosteoporotic drug effects,” *BoneKEy Rep.*, vol. 2, Dec. 2013, doi: 10.1038/bonekey.2013.181.

[24] E. A. Zimmermann, B. Busse, and R. O. Ritchie, “The fracture mechanics of human bone: influence of disease and treatment,” *BoneKEy Rep.*, vol. 4, Sep. 2015, doi: 10.1038/bonekey.2015.112.

[25] R. J. McBroom, W. C. Hayes, W. T. Edwards, R. P. Goldberg, and A. A. White, “Prediction of vertebral body compressive fracture using quantitative computed tomography.:,” *J. Bone Jt. Surg.*, vol. 67, no. 8, pp. 1206–1214, Oct. 1985, doi: 10.2106/00004623-198567080-00010.

[26] J. H. Keyak, J. M. Meagher, H. B. Skinner, and C. D. Mote, “Automated three-dimensional finite element modelling of bone: a new method,” *J. Biomed. Eng.*, vol. 12, no. 5, pp. 389–397, Sep. 1990, doi: 10.1016/0141-5425(90)90022-F.

[27] K. Ün and A. Çalık, “Relevance of inhomogeneous–anisotropic models of human cortical bone: a tibia study using the finite element method,” *Biotechnol. Biotechnol. Equip.*, vol. 30, no. 3, pp. 538–547, May 2016, doi: 10.1080/13102818.2016.1154803.

[28] “3D Slicer image computing platform,” 3D Slicer. Accessed: Mar. 27, 2023. [Online]. Available: https://slicer.org/

[29] “HOME | MOOSE.” Accessed: Mar. 27, 2023. [Online]. Available: https://mooseframework.inl.gov/

[30] “ParaView - Open-source, multi-platform data analysis and visualization application.” Accessed: Mar. 27, 2023. [Online]. Available: https://www.paraview.org/

[31] “CloudCompare.” 2023. [GPL software]. Available: http://www.cloudcompare.org/

[32] “RACCOON.” Accessed: Dec. 30, 2023. [Online]. Available: https://hugary1995.github.io/raccoon/index.html

[33] D. Paul, Z. Arwood, P.-Y. Mulon, D. Penumadu, and T. J. Truster, “Method for Computer Tomography Voxel-Based Finite Element Analysis and Validation with Digital Image Correlation System.” 2024. doi: 10.2139/ssrn.4863856.

[34] “CT Scanners Solutions Overview | Philips Healthcare,” Philips. Accessed: Jun. 14, 2024. [Online]. Available: https://www.usa.philips.com/healthcare/solutions/computed-tomography/ct-scanners

[35] E. M. C. Jones and M. A. (Eds.) Iadicola, *International Digital Image Correlation Society, Jones, E.M.C. and Iadicola, M.A. (Eds.) (2018). A Good Practices Guide for Digital Image Correlation. DOI: 10.32720/idics/gpg.ed1*. International Digital Image Correlation Society, 2018. [Online]. Available: DOI: 10.32720/idics/gpg.ed1

[36] C. E. Cann and H. K. Genant, “Precise measurement of vertebral mineral content using computed tomography.,” *J. Comput. Assist. Tomogr.*, vol. 4, no. 4, pp. 493–500, Aug. 1980, doi: 10.1097/00004728-198008000-00018.

[37] P. Ruegsegger and W. A. Kalender, “A phantom for standardization and quality control in peripheral bone measurements by PQCT and DXA,” *Phys. Med. Biol.*, vol. 38, no. 12, pp. 1963–1970, Dec. 1993, doi: 10.1088/0031-9155/38/12/018.

[38] A. Nazarian, B. D. Snyder, D. Zurakowski, and R. Müller, “Quantitative micro-computed tomography: A non-invasive method to assess equivalent bone mineral density,” *Bone*, vol. 43, no. 2, pp. 302–311, Aug. 2008, doi: 10.1016/j.bone.2008.04.009.

[39] H. Si, “TetGen, a Delaunay-Based Quality Tetrahedral Mesh Generator,” *ACM Trans Math Softw*, vol. 41, no. 2, Feb. 2015, doi: 10.1145/2629697.

[40] M. M. Goodsitt, “Conversion relations for quantitative CT bone mineral densities measured with solid and liquid calibration standards,” *Bone Miner.*, vol. 19, no. 2, pp. 145–158, 1992, doi: https://doi.org/10.1016/0169-6009(92)90922-Z.

[41] E. Schileo *et al.*, “An accurate estimation of bone density improves the accuracy of subject-specific finite element models,” *J. Biomech.*, vol. 41, no. 11, pp. 2483–2491, Aug. 2008, doi: 10.1016/j.jbiomech.2008.05.017.

[42] AO Research Institute, AO Foundation, Clavadelerstrasse 8, Davos, Switzerland, A. Pearce, R. Richards, S. Milz, E. Schneider, and S. Pearce, “Animal models for implant biomaterial research in bone: A review,” *Eur. Cell. Mater.*, vol. 13, pp. 1–10, Mar. 2007, doi: 10.22203/eCM.v013a01.

[43] J. H. Keyak, I. Y. Lee, and H. B. Skinner, "Correlations between orthogonal mechanical properties and density of trabecular bone: Use of different densitometric measures," *J. Biomed. Mater. Res.*, vol. 28, no. 11, pp. 1329–1336, Nov. 1994, doi: 10.1002/jbm.820281111.

[44] T. S. Keller, "Predicting the compressive mechanical behavior of bone," *J. Biomech.*, vol. 27, no. 9, pp. 1159–1168, Sep. 1994, doi: 10.1016/0021-9290(94)90056-6.

[45] "nglos324 - pmma." Accessed: Jun. 25, 2024. [Online]. Available: https://www.princeton.edu/~maelabs/mae324/glos324/pmma.htm

[46] G. Giudicelli *et al.*, "3.0 - MOOSE: Enabling massively parallel multiphysics simulations," *SoftwareX*, vol. 26, p. 101690, May 2024, doi: 10.1016/j.softx.2024.101690.

[47] J.-Y. Wu, V. P. Nguyen, C. T. Nguyen, D. Sutula, S. Sinaie, and S. Bordas, "Phase-field modeling of fracture," in *Advances in Applied Mechanics*, Elsevier, 2019, p. S0065215619300134. doi: 10.1016/bs.aams.2019.08.001.

[48] B. Bourdin, G. A. Francfort, and J.-J. Marigo, "Numerical experiments in revisited brittle fracture," *J. Mech. Phys. Solids*, vol. 48, no. 4, pp. 797–826, Apr. 2000, doi: 10.1016/S0022-5096(99)00028-9.

[49] J.-Y. Wu, "A unified phase-field theory for the mechanics of damage and quasi-brittle failure," *J. Mech. Phys. Solids*, vol. 103, pp. 72–99, Jun. 2017, doi: 10.1016/j.jmps.2017.03.015.

Vita

Debangshu Paul was born in Dhaka, Bangladesh, on October 25, 1990. He completed his Bachelor of Science in 2013 and Master of Science in 2016 in Mechanical Engineering from Bangladesh University of Engineering and Technology, Bangladesh. After finishing his bachelor, he served as a lecturer at Daffodil International University, Bangladesh for 2 years, and in May 2015, he joined the department of Compressor Research and Development, at Walton Hi-Tech Ind. Ltd. He served there for 7 years as the head of the Mechanical Design and Advanced Research section. In August 2022, he entered the University of Tennessee at Knoxville and received his master’s degree in Civil Engineering in August 2024.